Electromagnetic imaging of a dielectric micro-structure via convolutional neural networks

Peipei Ran
Laboratoire des Signaux et Systèmes
CNRS-CentraleSupélec-Univ. Paris Sud
Université Paris-Saclay
Gif-sur-Yvette, France
peipei.ran@l2s.centralesupelec.fr

Yingying Qin
Systèmes et Applications des Technologies de l'Information et de l'Energie
Ecole Normale Supérieure Paris-Saclay
Cachan, France
yingying.qin@ens-paris-saclay.fr
Laboratoire des Signaux et Systèmes
CNRS-CentraleSupélec-Univ. Paris Sud
Université Paris-Saclay
Gif-sur-Yvette, France
yingying.qin@l2s.centralesupelec.fr

Dominique Lesselier
Laboratoire des Signaux et Systèmes
CNRS-CentraleSupélec-Univ. Paris Sud
Université Paris-Saclay
Gif-sur-Yvette, France
dominique.lesselier@l2s.centralesupelec.fr

***Abstract*—Convolutional neural networks (CNN) are applied to the time-harmonic electromagnetic diagnostic of a dielectric micro-structure. The latter consists of a finite number of circular cylinders (rods) with a fraction of wavelength radius that are set parallel to and at sub-wavelength distance from one another. Discrete scattered fields are made available around it in a free-space multisource-multireceiver configuration. The aim is to characterize this micro-structure, like positions of rods or their absence, and in effect to map their dielectric contrasts w.r.t. the embedding space. A computationally efficient field representation based on a method of moments (MoM) is available to model the field. Iterative, sparsity-constrained solutions work well to find missing rods, but may lack generality and need strong priors. As for time-reversal and like noniterative solutions, they may fail to capture the scattering complexity. These limitations can be alleviated by relying on deep learning concepts, here via convolutional neural networks. How to construct the inverse solver is focused onto. Representative numerical tests illustrate the performance of the approach in typical situations. Comparisons with results from a contrast-source inversion (CSI) introduced in parallel are performed. Emphasis is on potential super-resolution in harmony with subwavelength features of the micro-structure.**

***Index Terms*—convolutional neural networks, micro-structure, super-resolution imaging, inverse scattering problem**

I. Introduction

Much attention is devoted nowadays to the characterization of micro-structures from electromagnetic fields which they may radiate or scatter. Without exhaustivity, examples have been analyzed in a strong mathematical framework [1], [2], yet corresponding computational approaches may be lacking still. Neural networks have been applied to inverse scattering since a long time [3], yet as computer resources increase, deep ones for real-time inverse scattering problems look promising.

The example investigated here is mapping a 2D cross-section of a finite-sized dielectric micro-structure exhibiting subwavelength features from time-harmonic scattered fields collected outside when illuminated in a multistatic mode of operation. It is prone to super-resolution since the elements in the micro-structure, as developed next, are subwavelength-sized and lie at subwavelengths from one another, and to map the microstructure at better than half-a-wavelength resolution thus is the key challenge and the main goal of the work.

The situation is simple enough to be appraised even if the underlying physics (e.g., possible occuring of open-cavity resonances) may not be so simple, yet is general enough to open the door to more demanding configurations, proven that the tools brought to the fore are fast, accurate and robust enough with the least amount of priors and constraints when employed.

The contribution is organized as follows. The scattering problem is detailed in section II. A deep learning procedure, inspired to an extent from [4], [5], involving convolutional neural networks (CNN), is set up and a convenient architecture of a network that applies to the present situation is provided in section III. How to handle the mapping via a well-known approach, the contrast-source inversion (CSI) [6], which yields a map of the dielectric contrast in a region of interest, is sketched in section IV —emphasize that there exist more powerful inversion tools, especially to deal with stronger contrasts, CSI is simply a handy tool among many options. Results of testing CNN on synthetic data are displayed in section V with comparison to those provided by CSI. A brief conclusion with outline of future works follows in section VI.

Notice that works involving two of the authors have been led on a similar scattering situation, but focus was on time-reversal and sparsity-based solutions in the peculiar case of looking for interior sources [7] or missing rods [8].

II. Formulation of the problem

The structure under study is sketched in Fig. 1. The scatterers consist of a finite number of infinitely-long circular cylindrical rods within a region of interest (ROI) in air with permittivity ϵ_0 and permeability μ_0. The radius of each rod is r, and the distance between two adjacent rods is d. Each rod is

978-9-0827-9703-9/19/$31.00

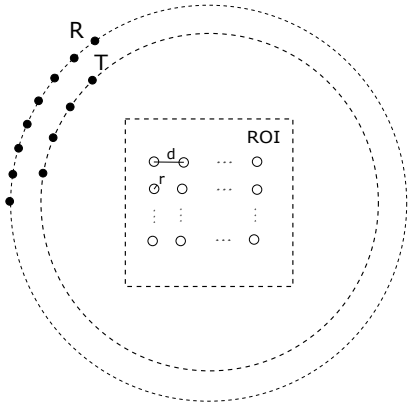

Fig. 1. Sketch of the inverse scattering problem, R represents the receiving antennas and T the transmitting antennas, rods are distributed in the ROI.

assumed to be homogeneous, isotropic and non-magnetic. Different rods may have different relative permittivities, denoted as $\epsilon_r(\mathbf{r})$. These scatterers are illuminated by time-harmonic transverse-magnetic waves generated by N_i ideal transmitters in turn at frequency of operation f. For each such illumination, the scattered fields are collected by N_r receivers on S. The inverse scattering problem is to determine shape, position, and dielectric properties in the ROI from those fields.

The scattering phenomenon can be appraised, as traditional, from two integral equations. The first one is the state equation, with only the pth transmitter illuminating the ROI,

$$E_p(\mathbf{r}) = E_p^{inc}(\mathbf{r}) + k_0^2 \int_D g(\mathbf{r},\mathbf{r}')\chi(\mathbf{r}')E_p(\mathbf{r}')d\mathbf{r}', \mathbf{r} \in D, \quad (1)$$

where $E_p(\mathbf{r})$ is the total electric field, $E_p^{inc}(\mathbf{r})$ is the incident field, k_0 is the wavenumber in air, and $g(\mathbf{r},\mathbf{r}')$ is 2-D scalar Green's function, $\chi(\mathbf{r})$ is the contrast defined as $\epsilon_r(\mathbf{r})-1$. The second equation is the observation equation

$$E_p^{sca}(\mathbf{r}) = k_0^2 \int_D g(\mathbf{r},\mathbf{r}')\chi(\mathbf{r}')E_p(\mathbf{r}')d\mathbf{r}', \mathbf{r} \in S, \quad (2)$$

where $E_p^{sca}(\mathbf{r})$ is the scattered field.

Retrieving the relative permittivities $\epsilon_r(\mathbf{r})(\mathbf{r} \in D)$ from measured scattered fields, $E_p^{sca}(\mathbf{r}), p = 1, 2, \ldots, N_i$, is nonlinear and ill-posed, and is usually cast into an optimization problem solved iteratively. A regularization strategy is often used to get a stable solution, thus the problem becomes

$$\text{Min} : f(\boldsymbol{\epsilon}_r(\mathbf{r})) = \sum_{p=1}^{N_i} \|F(\boldsymbol{\epsilon}_r, \mathbf{E}_p^{inc}) - \mathbf{E}_p^{sca}\|^2 + \gamma\|\boldsymbol{\epsilon}_r\|^2, \quad (3)$$

where F denotes the process of solving forward problem and Tikhonov regularization is standardly chosen as regularization method with the regularization parameter γ.

III. CNN INVERSE SCATTERING APPROACH

CNN have strong modeling capabilities and real-time reconstruction can be achieved when the network is well-trained. The network itself can realize the mapping from the scattered field to the distribution of the permittivity, thus there is no need of modeling. The proposed approach is detailed below.

A. CNN architecture design

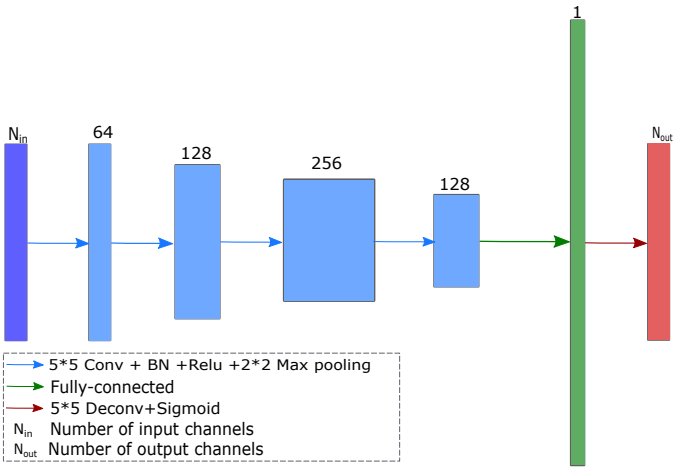

Fig. 2. Architecture of the proposed convolutional neural networks

The architecture as shown in Fig. 2 involves three main parts. The first part consists of three repeated blocks, and each block contains one 5×5 convolutional layer, one batch normalization (BN) layer, one rectified linear unit (ReLU) and a 2×2 max-pooling. The second part is a fully-connected layer, which combines all the information of the previous layer. It is important since every pixel in the reconstruction map is related to all the measured data. The last part is composed of one deconvolutional layer with a sigmoid activation function.

A convolutional layer has strong local modeling capabilities with a small number of parameters. BN is used to normalize the input layer and hidden layer by adjusting and scaling the activations, which can speed up the learning. ReLU, a non-saturated function, is chosen as the activation function to avoid vanishing gradients and to accelerate the convergence speed. Each convolutional layer is followed by a max pooling layer to reduce the data dimension. Using the deconvolutional layer is to generate an image representing the distribution of permittivity. To be mentioned, since the output range of the sigmoid function is $(0, 1)$, a linear transform is needed here so that the output range fits the range of permittivities.

B. Training data sets

The approach is evaluated on four different datasets: 2 configurations are set for both the number of the rods (16 vs. 36) and the permittivity range ([1, 2] vs. [1, 3]). The permittivity value of each rod is generated randomly, while the radius r and the distance d are kept constant, chosen as $\lambda/12$ and $\lambda/4$ respectively, with λ representing the wavelength in free space. Each training set contains 3000 samples, each one is collected from 72 receivers when illuminated by 36 transmitters at 3 GHz frequency set on circles of radius 0.76 m and of radius 0.72 m. For all datasets, the input of the network, namely the scattered field, is computed by a method of moments (MoM) with pulse basis and delta testing functions, corresponding with a ROI D divided into $M \times M$ square cells. Gaussian noise with SNR of 30 dB is added to the

synthetic data. In this work, only the real part of the scattered field is used as the input and as array of [36, 72]. Relative permittivities are exhibited according to the pixel basis as the expected output of the network with a shape of [50, 50]. We take another 100 samples to test the performance of the network for each case.

C. Loss function

The loss function combines the misfit between predictions and the ideal output of the network and a regularization term

$$LOSS = \frac{1}{N}\sum_{i=1}^{N}\|\boldsymbol{\epsilon}_r^i - \hat{\boldsymbol{\epsilon}}_r^i\|^2 + \alpha\sum_{j=1}^{P}\mathbf{W}_j^2, \tag{4}$$

in which N is the number of samples and P is the number of layers. For the ith sample, $\hat{\boldsymbol{\epsilon}}_r^i$ and $\boldsymbol{\epsilon}_r^i$ are the prediction value generated from the CNN and the ground truth, respectively. $\mathbf{W}_j$ are the weights of jth layer, and α is a hyper-parameter to balance the trade-off.

D. Training method

The network is trained by the Adam algorithm [9], which is an adaptive learning rate optimization algorithm designed specifically for training deep neural networks. It derives from optimization methods AdaGrad [10] and RMSProp [11]. Adam is more computationally efficient and the hyper-parameters are easy to choose. For completeness, it operates as follows:

Algorithm 1 ADAM optimization method

1: Initialize the biased first moment estimate and biased second raw moment estimate $\mathbf{m}_t = 0$, $\mathbf{v}_t = 0$;
2: Initialize the hyper-parameter $\beta_1 = 0.9$, $\beta_2 = 0.999$, $\delta = 10^{-8}$, β_1, β_2 are exponential decay rates;
3: Update $t = t + 1$; $\mathbf{m}_t = \beta_1\mathbf{m}_{t-1} + (1-\beta_1)\mathbf{g}_t$, $\mathbf{g}_t$ is the gradient of loss function w.r.t. $\mathbf{W}$;
4: Update $\mathbf{v}_t = \beta_2\mathbf{v}_{t-1} + (1-\beta_2)\mathbf{g}_t^2$;
5: Compute bias-corrected moment estimates, $\widehat{\mathbf{m}}_t = \mathbf{m}_t/(1-\beta_1^t)$, $\widehat{\mathbf{v}}_t = \mathbf{v}_t/(1-\beta_2^t)$;
6: Update the parameters $\mathbf{W}_t = \mathbf{W}_{t-1} - \alpha\mathbf{m}_t/(\sqrt{\widehat{\mathbf{v}}_t} + \delta)$, α is exponential decaying stepsize;
7: $\|\mathbf{W}_t - \mathbf{W}_{t-1}\|^2 < \xi$, stop, otherwise, repeat steps from 3 to 6.

IV. Iterative method - CSI Method

One of the most widely used methods to tackle an inverse scattering problem is the CSI method, refer to [6], which is based on source-type integral equations:

$$J_p(\mathbf{r}) = \chi(\mathbf{r})\left[E_p^{inc}(\mathbf{r}) + G_d(\mathbf{J}_p)\right], \mathbf{r} \in D, \tag{5}$$

$$E_p^{sca}(\mathbf{r}) = G_s(\mathbf{J}_p), \mathbf{r} \in S, \tag{6}$$

where the contrast source $J_p(\mathbf{r}) = \chi(\mathbf{r})E_p(\mathbf{r})$ is regarded as an independent parameter. $G_s(\cdot)$ and $G_d(\cdot)$ are operators defined as

$$G_s(\mathbf{J}_p) = k_0^2\int_D g(\mathbf{r},\mathbf{r}')J_p(\mathbf{r}')d\mathbf{r}', \mathbf{r} \in S, \tag{7}$$

$$G_d(\mathbf{J}_p) = k_0^2\int_D g(\mathbf{r},\mathbf{r}')J_p(\mathbf{r}')d\mathbf{r}', \mathbf{r} \in D. \tag{8}$$

The cost function here is a linear combination of normalized mismatches in the data equation and in the state equation.

$$\begin{aligned} L(\mathbf{J}_1,\ldots,\mathbf{J}_{N_i},\chi,\beta) = &\frac{\sum_{p=1}^{N_i}\|\mathbf{E}_p^{sca} - G_s(\mathbf{J}_p)\|^2}{\sum_{p=1}^{N_i}\|\mathbf{E}_p^{sca}\|^2} \\ &+ \beta\frac{\sum_{p=1}^{N_i}\|\chi\mathbf{E}_p^{inc} + \chi G_d(\mathbf{J}_p) - \mathbf{J}_p\|^2}{\sum_{p=1}^{N_i}\|\chi\mathbf{E}_p^{inc}\|^2}, \end{aligned} \tag{9}$$

Here we simply set $\beta = 1$ to give the two kinds of errors the same weight.

The cost function is minimized iteratively by alternately updating contrast source and contrast, thus there is no need to solve the forward problem and the optimization procedure becomes more efficient. The initial guesses for the two variables are calculated by backpropagation as [7]:

$$\mathbf{J}_p^{bp} = \frac{\|G_s^*(\mathbf{E}_p^{sca})\|^2}{\|G_s(G_s^*(\mathbf{E}_p^{sca}))\|^2}G_s^*(\mathbf{E}_p^{sca}), \tag{10}$$

$$\chi = \frac{\sum_{p=1}^{N_i}\mathbf{J}_p^{bp}\mathbf{E}_p^*}{\sum_{p=1}^{N_i}|\mathbf{E}_p|^2}, \tag{11}$$

where $\mathbf{E}_p = \mathbf{E}_p^{inc} + G_d(\mathbf{J}_p^{bp})$, $\mathbf{E}_p^*$ is the conjugate of $\mathbf{E}_p$ and $G_s^*(\cdot)$ is the adjoint operator of $G_s(\cdot)$.

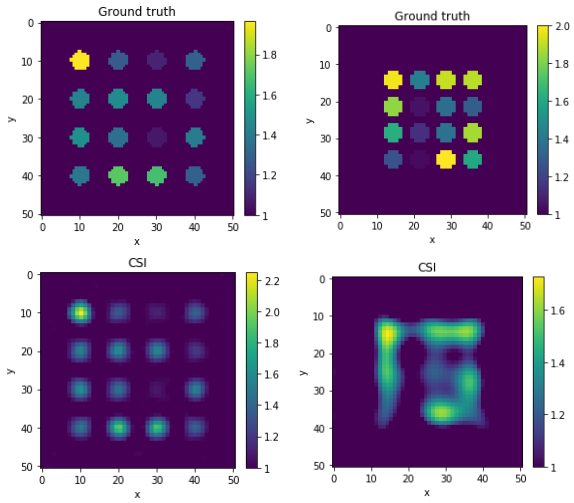

Fig. 3. Maps provided by CSI. Top to bottom: ground truth, CSI result. Left column $d = \lambda$ case, right column $d = \lambda/4$ case.

Here the contrast source is updated by a conjugate gradient method and then the contrast is calculated directly. Several tests have been performed to evaluate the CSI performance for different distances between rods, the relative error for each case being computed according to

$$ERR = \frac{1}{n}\sum_{i=1}^{n}\frac{\|\boldsymbol{\epsilon}_r^i - \hat{\boldsymbol{\epsilon}}_r^i\|^2}{\|\boldsymbol{\epsilon}_r^i\|^2}, \tag{12}$$

where n is the number of test samples.

Illustrative errors are given in Table I. CSI maps with $d = \lambda$ and with $d = \lambda/4$ are displayed in Fig. 3; the latter illustrate that CSI can achieve a rather good result when the distance between rods is equal to or larger than λ, but fails when the rods are closer to one another. In contrast, the CNN-based method can succeed in that case, as shown thereafter.

TABLE I
ERRORS OF RECONSTRUCTION ERR USING CSI

distance between rods: d	$\lambda/4$	$\lambda/2$	λ	2λ
relative error	0.0282	0.0032	0.0011	5.7 10^{-5}

V. RESULTS

Table II shows the relative error ERR of CNN for $d = \lambda/4$, in which case CSI cannot achieve good reconstruction, in four different cases, in which the highest relative error is 0.00452. Fig. 4 offers two examples of a 16-rod case, one for the lower permittivity and one for the higher permittivity, and Fig. 5 offers two examples of a 36-rod case, one for the lower permittivity and one for the higher permittivity.

TABLE II
ERRORS OF RECONSTRUCTION ERR USING CNN FOR $d = \lambda/4$

relative permittivity	**1-2**	**1-3**
Example of 16 rods	0.00275	0.00116
Example of 36 rods	0.00446	0.00449

Overall, CNN achieves an accurate permittivity reconstruction in the four cases studied, both in terms of localization of rods and retrieval of their contrasts with respect to the embedding and to one another, even if with noisy data as used. In effect ground truth and the retrieved map are almost indistinguishable, as epitomized by the square-norm errors correspondingly provided. The implementation is based on TensorFlow, the batch size is set to 100 and the learning is stopped after 6000 iterations (200 epochs). The GPU that we use is NVIDIA GEFORCE GTX 1080, which takes about 14 minutes for the training of the network. With a well-trained network, it takes less than 1 second to get the evaluation of contrast map, which means that a real-time diagnostic is achieved.

As for CSI, as mentioned in the above, it mostly fails to capture the dielectric distribution of the micro-structure, some rods appear here and there, but there is no rule in that, whereas the maximum contrast values reached are less than the true ones. But we should emphasize that a priori information of these two methods are different.

Other examples, with different micro-structures in terms of contrast, number, size and inter-distance of the rods, and with different measurement configurations encompassing aspect-limited data in particular, will be shown at the time of presentation.

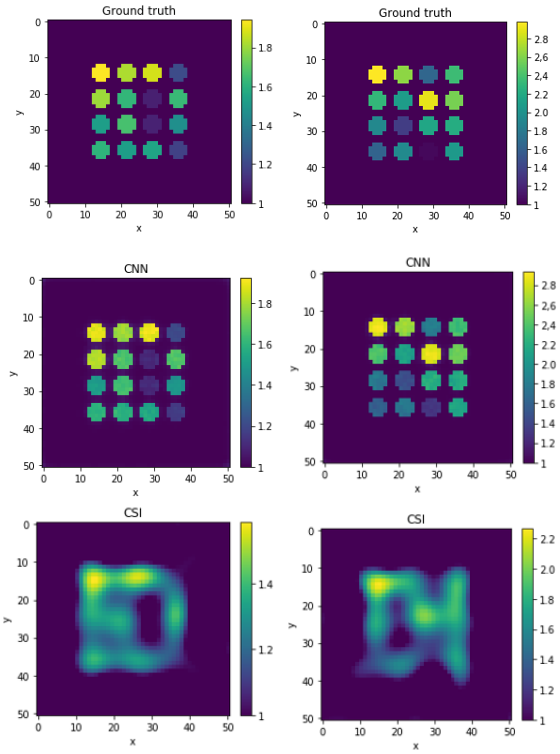

Fig. 4. Maps provided by CNN compared with those provided by CSI for examples involving 16 rods. Top to bottom: ground truth, CNN result, CSI result. Left column: Example 1 with lower permittivity. Right column: Example 2 with higher permittivity.

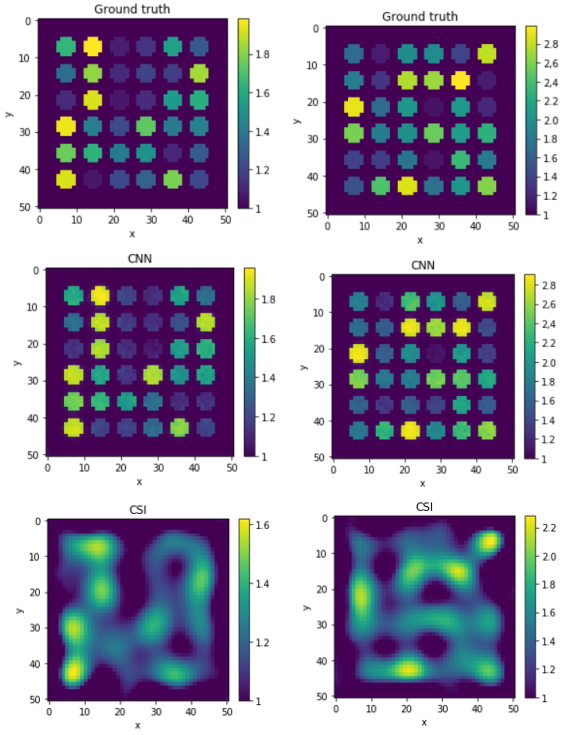

Fig. 5. Maps provided by CNN compared with those provided by CSI for examples involving 36 rods. Same as in Fig. 4.

VI. Conclusion

Imaging of a dielectric micro-structure has been investigated. With respect to an implementation of contrast-source inversion, an inverse solver based on convolutional neural networks exhibits super-resolution features in the sense that the fact that the structure is subwavelength both in terms of size of elements and inter-element distance does not impair its mapping. Also it applies to a wide range of geometrical and electrical properties of the elements, which may not be possible if one uses sparsity-constrained methods as recently proposed [12], while it does not suffer from intrinsic limitations of backpropagation-based methods. Obviously good care must be taken so as to avoid that the neural network becomes too much tuned to a given situation, and then loses generality. Yet the same could be said with contrast-source inversion, used as reference here, with the more constraints enforced, the better results expected.

The case considered here is avowedly limited in terms of scattering phenomenon since reduced to a two-dimensional transverse-magnetic scalar one, yet the approach is not limited to it. A full three-dimensional vector wave situation in which rods are now finite in length has been considered as of recently, with specialization to metallic rods [8] for which resonances can appear in specific wavebands and thus facilitate super-resolution. The main hurdle here is not about devising the networks but to achieve a direct even approximated fast computational modeling of the fields. Investigations along that direction, now both from synthetic and experimental data in anechoic chambers, will be led in the near future.

References

[1] H. Ammari, J. Garnier, W. Jing, H. Kang, M. Lim, K. Sølna, and H. Wang, Mathematical and Statistical Methods for Multistatic Imaging, Berlin: Springer, 2013.

[2] H. Ammari and H. Zhang, “A mathematical theory of super-resolution by using a system of sub-wavelength Helmholtz resonators,” Commun. Mathemat. Phys., vol. 337, pp. 379-428, 2015.

[3] S. Caorsi and P. Gamba, “Electromagnetic detection of dielectric cylinders by a neural network approach,” IEEE Trans. Geosci. Remote Sens., vol. 37, pp. 820-827, 1999.

[4] Z. Wei and X. Chen, “Deep-learning schemes for full-wave nonlinear inverse scattering problems,” IEEE Trans. Geosci. Remote Sens., vol. 57, pp. 1849-1860, 2019.

[5] A. Lucas, M. Iliadis R. Molina, and A. K. Katsaggelos, “Using deep neural networks for inverse problems in imaging: beyond analytical methods,” IEEE Signal Proc. Mag., vol. 35, pp. 20-36, 2018.

[6] X. Chen, Computational Methods for Electromagnetic Inverse Scattering, 1st. ed.: Wiley-IEEE Press, 2018.

[7] H. Tu, M. Serhir, P. Ran, and D. Lesselier, “On the modeling and diagnosis of a microstructured wire antenna system,” IEEE Proc. 2018 International Conference on Microwave and Millimeter Wave Technology (ICMMT), Chengdu, May 2018.

[8] P. Ran, Z. Liu, D. Lesselier, and M. Serhir, “Diagnostic within a dielectric micro-structure: time-reversal and sparsity-constrained imaging,” IEEE Proc. 13th European Conference on Antennas and Propagation (EUCAP), Krakow, April 2019, in press.

[9] D. P. Kingma and J. Ba, “Adam: A method for stochastic optimization,” 3rd International Conference for Learning Representations, San Diego, May 2015. arxivr 1412.6980.

[10] J. Duchi, E. Hazan, and Y. Singer, “Adaptive subgradient methods for online learning and stochastic optimization,” J. Mach. Learn. Res., vol. 12, pp. 2121-2159, 2011.

[11] T. Tieleman and G. Hinton, Lecture 6.5-RMSProp, COURSERA: Neural networks for machine learning technical report, 2012.

[12] Z. Liu, D. Lesselier, and Y. Zhong, ”Electromagnetic imaging of damages in fibered layered laminates via equivalence theory,” IEEE Trans. Comput. Imag., vol. 4, pp. 219-227, 2018.